Full Length Article

Ultrafast synthesis of cobalt/carbon nanocomposites by magnetic induction heating for oxygen evolution reaction

Qiming Liu [a], Samuel McNair [b], Forrest Nichols [a], Bingzhang Lu [a], Bingzhe Yu [a], Dingjie Pan [a], Jamie Ko [b], Amrinder Bhuller [a], Frank Bridges [b], Shaowei Chen [a,*]

[a] Department of Chemistry and Biochemistry, University of California, 1156 High Street, Santa Cruz, CA, 95064, United States
[b] Department of Physics, University of California, 1156 High Street, Santa Cruz, CA, 95064, United States

ABSTRACT

Metal/carbon nanocomposites have shown great potential as high-performance, low-cost electrocatalysts owing largely to their unique metal-support interactions. These nanocomposites are typically prepared by conventional pyrolysis that is tedious and energy-intensive. Herein, we report the ultrafast preparation of cobalt/carbon nanocomposites by magnetic induction heating (MIH) of metal organic frameworks within seconds under an inert atmosphere. The resulting samples consist of cobalt nanoparticles encapsulated within defective carbon shells, and effectively catalyze oxygen evolution reaction (OER) in alkaline media. Among the series, the sample prepared at 400 A for 10 s exhibits the best OER performance, needing a low overpotential of $+308$ mV to reach the current density of 10 mA cm^{-2}, along with excellent stability, and even outperforms commercial RuO$_2$ at high overpotentials. This is ascribed to the charge transfer between the carbon scaffold and metal nanoparticles. Operando X-ray absorption spectroscopy measurements show that the electrochemically produced CoOOH species is responsible for the high electrocatalytic performance. The results highlight the unique potential of MIH in the development of effective nanocomposite catalysts for electrochemical energy technologies.

1. Introduction

Natural gas reforming accounts for 95% of the hydrogen gas produced in the United States; yet the hydrogen is non-sustainable and "grey", as it originates from fossil fuels [1]. To obtain sustainable "green" hydrogen gas, electrochemical water splitting by using renewable electricity has emerged as one of the most promising technologies, which consists of hydrogen evolution reaction (HER) at the cathode and oxygen evolution reaction (OER) at the anode [2]. Yet, due to the sluggish electron-transfer kinetics and complex reaction pathways, OER typically entails a large overpotential and severely hampers the overall efficiency of the water electrolyzers [3]. Iridium and ruthenium-based nanoparticles have been the leading catalysts for OER; yet their natural scarcity and high costs have made widespread applications impractical [4–6]. Thus, extensive research has been carried out to develop efficient alternatives, such as metal alloys [7–9], metal oxides [10–13], hydrides [14,15], oxy-hydroxides [16,17], sulfides [8,18], phosphides [4,19], etc.

Recently, metal/carbon nanocomposites have also been attracting intensive attention [20–23], owing to their high electrical conductivity and strong metal-support interactions (e.g., charge transfer between

carbon and metal, spatial confinement by encapsulation). For example, Cui et al. [24] prepared a series of nanocomposites with non-noble metal nanoparticles (e.g., Fe, Co, Ni, and their alloys) encapsulated within single-layer graphene, in which FeNi showed the best OER activity with an overpotential (η_{10}) of $+280$ mV at 10 mA cm^{-2} in alkaline media. Theoretical studies based on density functional theory (DFT) calculations showed that electron transfer occurred from the metal cores to the graphene layer and significantly altered the adsorption energetics of oxygen species on the graphene surface, leading to an enhanced OER performance. Yang et al. [25] prepared FeCoNi ternary nanoalloys encapsulated in N-doped graphene layers by direct annealing of Prussian blue, which showed a low η_{10} of $+288$ mV towards OER in alkaline media. Similarly, they found that charge transfer from the metals to graphene lowered the energy barrier of OER electrochemistry. In these studies, the metal/carbon nanocomposites are prepared via a variety of strategies, including pyrolysis of metal-organic frameworks (MOFs) [26], chemical vapor deposition (CVD) [27], electrospun nanofibers [28], wet chemistry [29,30], etc. These procedures, while effective, are in general tedious (of the order of hours) and may need sophisticated instrumentation [31–33].

* Corresponding author.
  E-mail address: shaowei@ucsc.edu (S. Chen).

Such issues can be mitigated by the recent emergence of ultrafast synthesis, e.g., carbothermal shock, flash Joule heating, laser ablation, and magnetic induction heating (MIH) [21,34–38]. These techniques can not only cut down the sample preparation time to (milli)seconds but also create non-equilibrium structures, such as stacking faults, point defects, and high-entropy mixtures, that are unattainable in conventional methods [34]. For instance, Meng et al. [39] utilized a laser to heat a cobalt target in liquid, and produced CoOOH with abundant oxygen vacancies, owing to the ultrafast heating rate. The resulting defective CoOOH exhibited an η_{10} of +330 mV for OER, much better than bulk CoOOH without oxygen vacancies. In another study, Cui et al. [18] prepared high-entropy metal sulfide (CrMnFeCoNi)S$_x$ nanoparticles by using carbothermal shock for just 55 ms, and observed a high OER performance with a low overpotential (η_{100}) of +295 mV to reach a high current density of 100 mA cm^{-2}. Recently, we demonstrated that MIH could also be exploited for the ultrafast synthesis of high-performance electrocatalysts [35,36]. MIH is a traditional metallurgical tool, whereupon the application of a high-frequency AC current to the solenoid, a strong magnetic field is generated, which instantly produces a high Eddy current in the conductors within the field and heats the sample rapidly to a high temperature. In one recent study [36], FeNi spinel nanostructures were produced within seconds featuring a homogenous mixing of the Fe and Ni phases and substantial Cl residuals, both of which were difficult to obtain in conventional methods and contributed collectively to a remarkable OER performance ($\eta_{100} = +260$ mV). In another study [35], ruthenium nanoparticles supported on carbon paper were prepared by MIH, where the surface Cl residuals were found to be responsible for the high HER activity ($\eta_{10} = -23$ and -12 mV in acidic and alkaline media, respectively) that was highly comparable to that of commercial Pt/C benchmark. Nevertheless, despite the progress to date, very few studies have focused on the controllable synthesis of metal/carbon nanocomposites by ultrafast synthesis [34,40].

Herein, we prepared a series of cobalt/carbon nanocomposites by MIH treatment for 10 s [35,36] of zeolitic imidazolate frameworks-67 (ZIF-67), where cobalt nanoparticles were encapsulated within defective N-doped carbon shells. Owing to the different degrees of carbonization (by controlling the magnetic induction current), various amounts of Co species were exposed to the electrolytes, which effectively impacted the OER activity. Amongst the series, the sample prepared at the applied current of 400 A showed the best OER performance in alkaline media, with a low η_{10} of +308 mV and η_{200} of +410 mV, a performance even higher than that of commercial RuO$_2$ in the high overpotential range. Operando X-ray absorption spectroscopy measurements showed that the excellent activity was due to the formation of CoOOH on the carbon shell surface, likely due to electrochemical decomposition of the encapsulated metallic nanoparticles.

2. Experimental section

2.1. Synthesis of ZIF-67

In a typical synthesis [30], 1.092 g of Co(NO$_3$)$_2$·6H$_2$O was dissolved in 30 mL of methanol in a vial, and 1.232 g of 2-methylimidazole in 30 mL methanol in another vial. These two solutions were mixed under sonication for 10 min to form a purple solution. The solution was then transferred to a 100 mL Teflon-lined stainless-steel autoclave and heated at 120 °C for 2 h, producing a purple precipitate that was collected via centrifugation at 6000 r min^{-1} for 5 min, rinsed three times with methanol, and dried under vacuum at 50 °C for 12 h. The obtained product was the ZIF-67 crystals.

2.2. MIH synthesis

Carbon paper was thermally treated in a muffle furnace at 500 °C in ambient for 1 h to increase surface wettability, cut into 1 × 2 cm^2 pieces, and rinsed with acetone several times. The ZIF-67 produced above was sonicated and dispersed into ethanol at a concentration of 60 mg mL^{-1}, 100 μL of which was then dropcast onto the carbon paper. After drying in air for 30 min, the carbon paper was put on an iron sheet (2.5 cm × 2.5 cm × 0.2 mm) covered with a piece of graphite paper (0.01 mm thick) to prevent contamination from iron, and the assembly was placed on the center of a firebrick inside a quartz tube that was purged with high-purity Ar gas for 10 min. The quartz tube was then set into a four-turn induction coil with a diameter of 5 cm, and MIH was carried out at a controlled current (X = 200–600 A) for a heating time of 10 s before the sample was naturally cooled down to room temperature. The resulting samples were denoted as Co-NC-X.

2.3. Characterizations

Transmission electron microscopy (TEM) images were acquired with a Tecni G2 operated at 200 kV. X-ray photoelectron spectroscopy (XPS) measurements were carried out with a Thermo Fisher K-alpha system, where the binding energy was calibrated against the C 1s binding energy. Raman measurements were conducted using a Horiba Jobin Yvon Lab-RAM ARAMIS automated scanning confocal Raman microscope under 532 nm excitation. Ex situ X-ray absorption spectroscopy (XAS) measurements were carried out at 10 K at beamline 4–1 of the Stanford Synchrotron Radiation Lightsource using an Oxford liquid helium cryostat. Operando XAS measurements were carried out at room temperature in a homemade cell.

2.4. Electrochemistry

Electrochemical measurements were carried out with a CHI 700E electrochemical workstation in a three-electrode configuration. The obtained carbon paper was fixed onto a graphite electrode holder, with an exposed surface area of 1 cm^2. A graphite rod was used as the counter electrode and a Hg/HgO in 1 M KOH as the reference electrode. The reference electrode was calibrated against a reversible hydrogen electrode (RHE) and all potentials in the present study were referenced to this RHE. Commercial RuO$_2$ was dropcast onto a carbon paper for benchmarking at the same metal loading.

3. Results and discussion

3.1. Sample preparation and structural characterizations

As shown in Fig. 1a, the preparation of Co-NC nanocomposites by MIH treatment of ZIF-67 consists of two major steps [35,36]. First, ZIF-67 was synthesized and dropcast onto a piece of carbon paper (ZIF-67/CP), which was then put onto an iron sheet covered with a piece of graphite paper (Fig. S1a). The assembly was inserted into a quartz tube purged with Ar gas, which was placed into the center of a solenoid (Fig. 1b). Upon the application of an AC current, the surface of the iron sheet was heated up quickly to over 1000 °C within seconds (Fig. 1c), owing to the Joule's heating effect. At the induction current of 300 A or higher for just 10 s, ZIF-67 was thermoradiatively converted into Co-NC nanocomposites with Co nanoparticles encapsulated within N-doped carbon, as manifested with a rapid color change from purple to black; whereas at a lower current of only 200 A, the sample retained the purple color, signifying incomplete decomposition of ZIF-67 as the MIH temperature was too low (Fig. S1b-c). Five samples were prepared at a controlled induction current (X = 200–600 A), and denoted as Co-NC-X (Fig. S1c).

The sample structures were first characterized by TEM measurements. From Fig. 2a–e and Figs. S2-S5, it can be seen that upon MIH treatment at 200–600 A for 10 s, nanocomposites were produced where dark-contrast nanoparticles (dia. 5–10 nm) were embedded within a low-contrast scaffold, and the number of nanoparticles increased with increasing induction current, leading to an increasingly roughened morphology. For Co-NC-200 that retained the rhombic dodecahedral shape of ZIF-67 with a size of about 500 nm (Fig. 2a), the relatively low
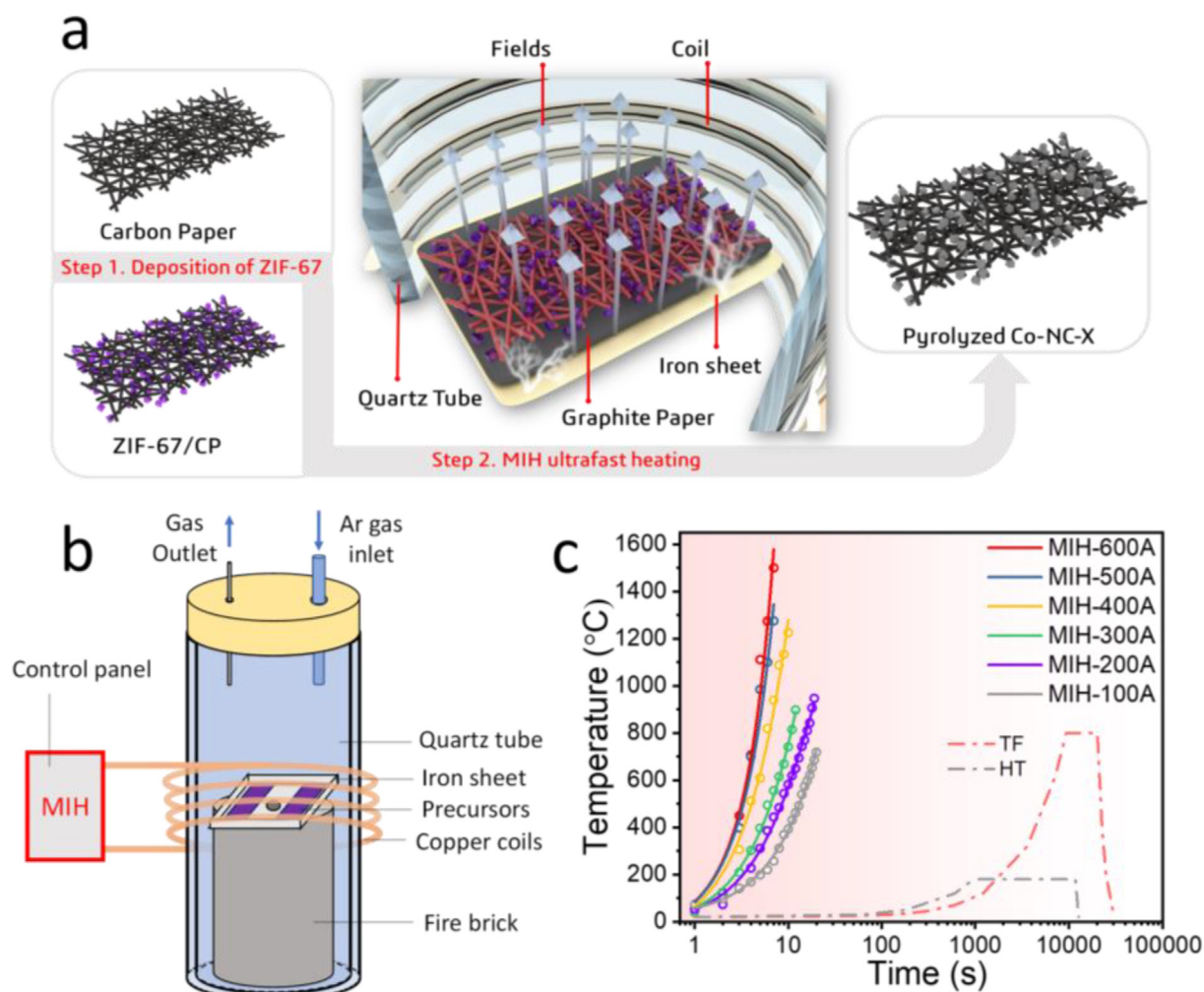
Fig. 1. (a, b) Schematic illustration of ultrafast pyrolysis of ZIF-67 by MIH, where CP denotes carbon paper. (c) Heating temperature as the function of time by using MIH at different heating currents, as determined with an infrared thermometer. TF and HT denote conventional tube furnaces and hydrothermal methods, respectively.

current (and hence temperature, ca. 500 °C) led to only incomplete decomposition of ZIF-67 (Fig. S1c), thus the number of nanoparticles was low [41]. In high-resolution TEM measurements (Fig. 2f and Fig. S2), crystalline lattice fringes can be found in both the nanoparticles and the low-contrast scaffold, with an interplanar spacing of 0.416 and 0.269 nm, which can be ascribed to the enlarged (002) facet of graphitic carbon (owing to the formation of abundant interplanar sp^3 C) [42] and the (111) facet of cubic CoO (JCPDS #43–1004), respectively. When the induction current was increased to 300 A, a higher temperature was reached at ca. 700 °C, which led to the production of a number of metallic Co and CoO nanoparticles encapsulated within a rather thick amorphous carbon layer (Fig. 2b and g and Fig. S3). The number of nanoparticles became even higher for the Co-NC-400 (Fig. 2c, h and k–m), Co-NC-500 (Fig. 2d and i, and Fig. S4) and Co-NC-600 (Fig. 2e and j, and Fig. S5) samples that were prepared at even higher induction currents (temperatures). In addition, one can see that the metallic Co domain size increased whereas that of CoO diminished from Co-NC-200 to Co-NC-600, suggesting that CoO was likely the structural intermediate during the thermal conversion of ZIF-67 to cobalt nanoparticles (vide infra).

The lattice spacing of the carbon scaffold also exhibited a dynamic evolution. For the samples prepared at relatively low induction currents (i.e., Co-NC-200, Co-NC-300, and Co-NC-400) (Fig. 2f–h), the carbon scaffold can be seen to exhibit a rather consistent d spacing of 0.412 nm, which is markedly larger than that (0.350 nm) observed with Co-NC-500

(Fig. 2i) and Co-NC-600 (Fig. 2j). This suggests enhanced graphitization of the latter due to a markedly higher heating temperature (up to 1500 °C) and largely defective carbon layers in the former.

XPS measurements were then performed to examine the chemical compositions and valence states of the samples. From the survey spectra in Fig. S6, the samples can be seen to consist of only C, N, and Co (Tables S1-S5), suggesting successful conversion of ZIF-67 to Co-NC nanocomposites by MIH treatment. Fig. 3a shows the high-resolution scans of the C 1s electrons in the series of samples. One can find that the C 1s spectrum of Co-NC-200 can be deconvoluted into two components, sp^2 C of the imidazole rings at 284.6 eV and sp^3 C of the methyl groups at 285.8 eV, indeed suggesting incomplete decomposition of the ZIF-67 precursor [43,44]. For samples prepared at higher induction currents, the C 1s spectra can be found to consist of three components, sp^2 C at ca. 284.0 eV, sp^3 C at ca. 284.8 eV, and oxidized C at ca. 288.0 eV. This suggests that 2-methyimidazole in ZIF-67 was gradually decomposed and evolved into sp^2 C of the graphitic carbon layers. This was also manifested by the change of the sp^2 C/sp^3 C ratio (Fig. 3e), which increased from 0 for Co-NC-200 to 1.0 for CO-NC-300, and finally to ca. 1.2 for Co-NC-400, Co-NC-500, and Co-NC-600. The increasing graphitization of the carbon shells over Co and CoO nanoparticles was also manifested by the increasing surface content of C from 70.02 at% of Co-NC-200 to 73.91 at% for Co-NC-300, 77.31 at% for Co-NC-400, 81.54 at% for Co-NC-500 and 86.81 at% for Co-NC-600 (Fig. 3e, Tables S1-S5).
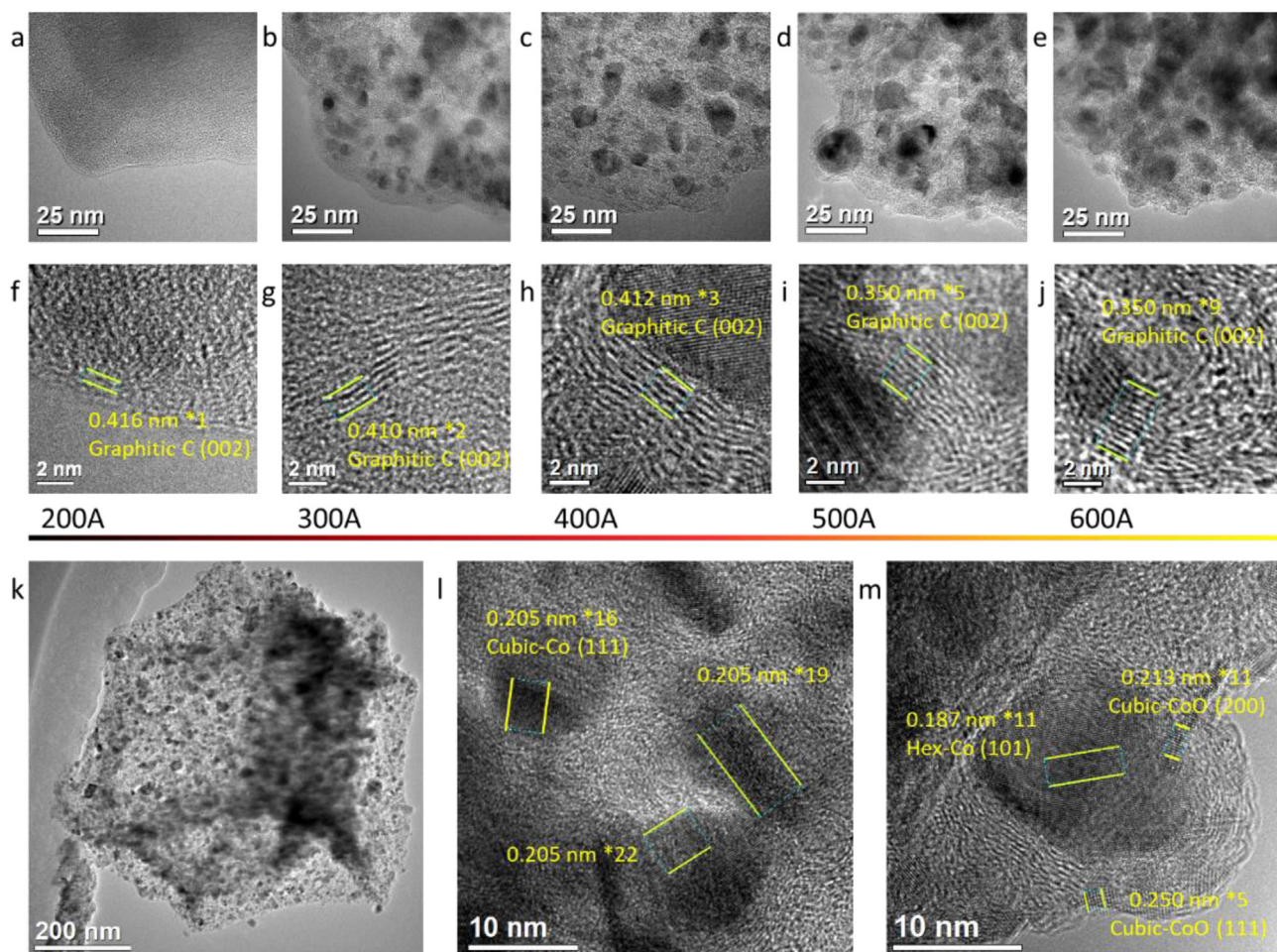
Fig. 2. Representative TEM images of (a, f) Co-NC-200, (b, g) Co-NC-300, (c, h) Co-NC-400, (d, i) Co-NC-500, and (e, j) Co-NC-600. (k–m) TEM images of Co-NC-400 at different magnifications where the various lattice fringes are highlighted.

Consistent results were obtained in Raman measurements. From Fig. 3f, Co-NC-200 can be seen to exhibit only a featureless baseline in the range of 1000–2000 cm^{-1}, suggesting no well-defined graphitic structure. By contrast, both Co-NC-400 and Co-NC-600 exhibited two prominent peaks at 1333 cm^{-1} (D band) and 1580 cm^{-1} (G band), due to the out-of-plane (i.e., defects) and in-plane vibrations, respectively [45]. Furthermore, the intensity ratio of these two bands (I_D/I_G) decreased somewhat from 1.03 for Co-NC-400 to 0.93 for Co-NC-600, consistent with increasing graphitization of the samples prepared at increasing induction currents (Fig. 2f–j).

The N 1s spectra are depicted in Fig. 3b. One can see that Co-NC-200 consists of a main peak at 398.8 eV, due to the N atoms of 2-methylimidazole [43]. For other samples, three N species can be resolved, pyridinic N at ca. 398.1 eV, pyrrolic N at ca. 400.1 eV, and oxidized N (over 401.5 eV), signifying the successful doping of N into the carbon skeletons likely by deamination of the imidazole rings and formation of graphitic C rings during ultrafast heating [46]. Notably, one can see from Fig. 3g that with increasing heating currents, the overall content of the N species decreased monotonically from 18.16 at% for Co-NC-200 to 10.90 at% for Co-NC-300, 7.96 at% for Co-NC-400, 6.64 at% for Co-NC-500, and 4.73 at% for Co-NC-600, whereas concurrently the content of pyrrolic N increased from 1.34 at% for Co-NC-200 to 1.90 at% for Co-NC-300, 1.76 at% for Co-NC-400, 1.33% for Co-NC-500, and 2.97 at% for Co-NC-600 (Table S1-S5), signifying that pyrrolic N became the increasingly dominant species in the sample series. Such a trend is contradictory to results in traditional pyrolysis in that pyrrolic N is energetically unstable at high temperatures [47]. This suggests that MIH might be a unique tool to create metastable N-doped carbon structures.

Fig. 3c shows the corresponding high-resolution scans of the Co 2p electrons. One can see that Co-NC-200 consisted of a doublet at 781.1/796.7 eV arising from the $2p_{3/2}/2p_{1/2}$ electrons of Co^{2+} species and a pair of satellite peaks at 785.9/802.6 eV [48,49]. For other samples (i.e., X = 300, 400, 500, and 600 A), an additional doublet appeared at 777.8/793.5 eV, which can be assigned to the $2p_{3/2}/2p_{1/2}$ electrons of metallic Co [50]. This is consistent with the results from TEM measurements where both Co and CoO lattice fringes were observed (Fig. 2 and Figs. S2-S5). In fact, the Co^{2+} content can be found to diminish markedly from ca. 5.53 at% for Co-NC-200 to 4.16 at% for Co-NC-300, 4.20 at% for Co-NC-400, 3.18 at% for Co-NC-500 and 2.21 at% for Co-NC-600, whereas the content of metallic Co was the highest with Co-NC-600 at 0.48 at%, in comparison to ca. 0.2 at% for Co-NC-500, Co-NC-400 and Co-NC-300, and undetectable in Co-NC-200 (Fig. 3h, Tables S1-S5). In addition, one can see that the Co^{2+} $2p_{3/2}$ binding energy (red dashed line in Fig. 3c) red-shifted from 781.1 eV for Co-NC-200 to 779.9 eV for Co-NC-300, 780.1 eV for Co-NC-400, 779.7 eV for Co-NC-500, and further to 779.3 eV for Co-NC-600 (Tables S1-S5). This suggests increasing charge transfer from the carbon scaffold to Co^{2+} species (CoO or CoN_x moieties), which facilitated the reduction of Co^{2+} to metallic Co, due to enhanced graphitization at elevated temperatures [51].

High-resolution scans of the O 1s electrons further confirm the formation of CoO species except for Co-NC-200. From Fig. 3d, one can see that no peak around 529–530 eV can be discerned in the O 1s spectrum of Co-NC-200, whereas for other samples in the series, the peak (purple color) can be readily deconvoluted due to metal oxide (O_{metal}) [36]. In fact, it can be seen from Fig. 3h and Tables S1-S5 that the O_{metal} content increased from 0 at% for Co-NC-200 to 0.86 at% for Co-NC-300, 1.44 at%
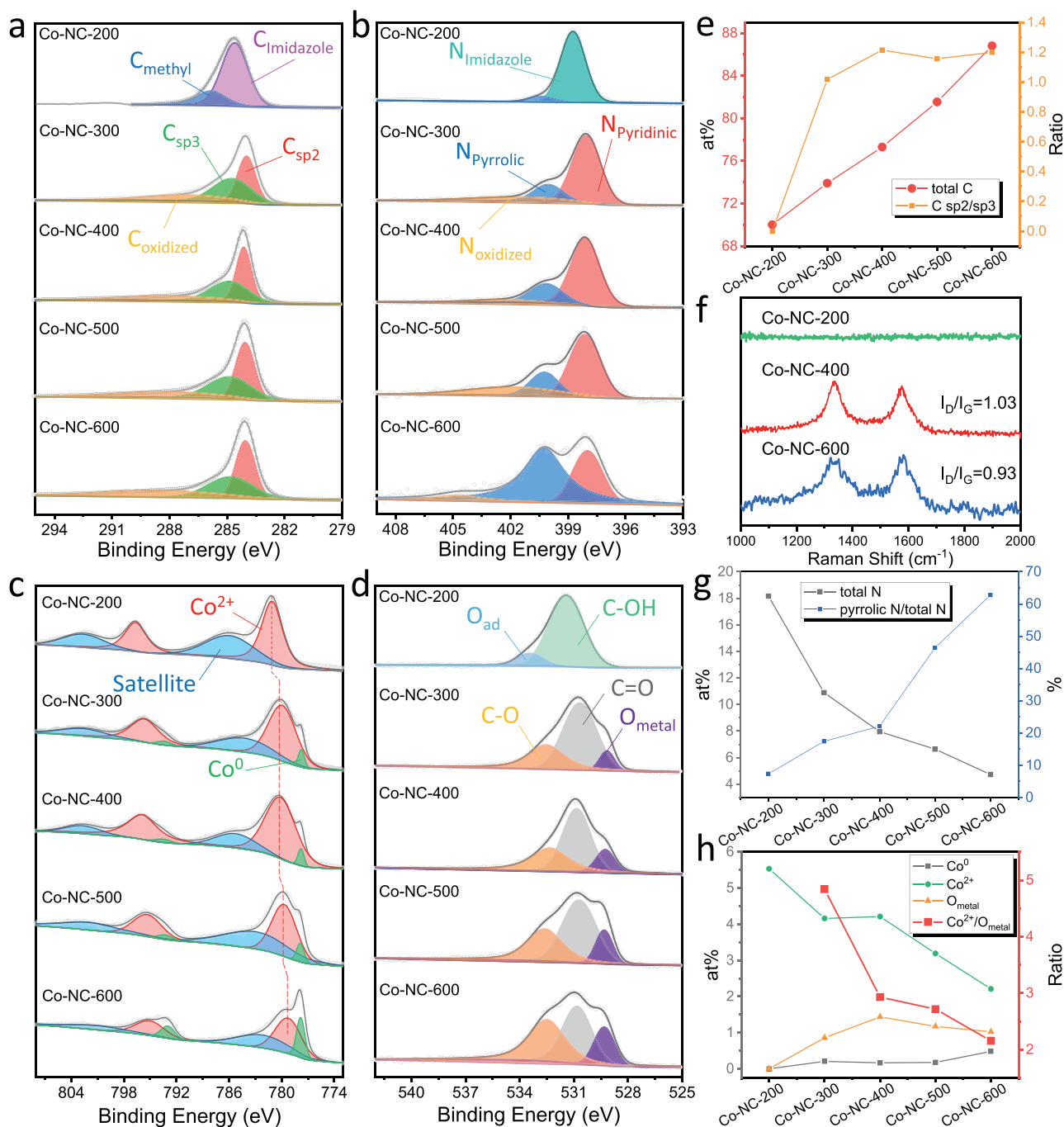
Fig. 3. High-resolution scans of the (a) C 1s, (b) N 1s, (c) Co 2p, and (d) O 1s electrons of Co-NC-200, Co-NC-300, Co-NC-400, Co-NC-500, and Co-NC-600. (e) Carbon contents derived from XPS measurements. (f) Raman Spectra of Co-NC-200, Co-NC-400, and Co-NC-600. (g) Contents of total N and pyrrolic N derived from XPS measurements. (h) Variation of the contents of different Co and O species.

for Co-NC-400, and then decreased to 1.17 at% for Co-NC-500 and 1.02 at% for Co-NC-600. Interestingly, the atomic ratio between Co^{2+} and O_{metal} decreased from 4.8 for Co-NC-300 to 2.9 for Co-NC-400, 2.7 for Co-NC-500 and 2.2 for Co-NC-600 (Fig. 3h). The fact that all are higher than the stoichiometric ratio (1:1) of CoO suggests the formation of CoN_x moieties [49], which likely decomposed at high temperatures, due to the loss of the N dopants (Fig. 3g), and aggregated into CoO/Co nano-particles in the carbon matrix.

Further structural insights of the samples were obtained from XAS measurements. Fig. 4a depicts the Co K-edge X-ray absorption near edge spectra (XANES) of the sample series, Co foil, and CoOOH. One can see that Co-NC-200, Co-NC-400, and Co-NC-600 all exhibited an absorption edge between those of Co foil and CoOOH, suggesting an average valence state between 0 and + 3, which is consistent with the XPS results (Fig. 3). Meanwhile, both Co-NC-400 and Co-NC-600 showed a pre-edge feature similar to that of Co foil at 7713 eV, confirming the formation of metallic Co in the samples, while Co-NC-200 possessed a sharp pre-edge peak at 7710 eV, due to the 1s → 3d transitions of tetrahedral $Co^{II}–N_4$ [52,53]. Fig. 4b shows the corresponding extended X-ray absorption fine structures (EXAFS) of the samples. One can see that none of the Co-NC samples exhibited a profile resembling that of CoOOH (which consisted of two prominent peaks at 1.43 and 2.50 Å due to Co–O and Co–Co, respectively) [54]. Specifically, Co-NC-200 displayed a main peak at 1.55 Å, due to the Co–N/O bonds of the ZIF-67 precursor; and this peak became a
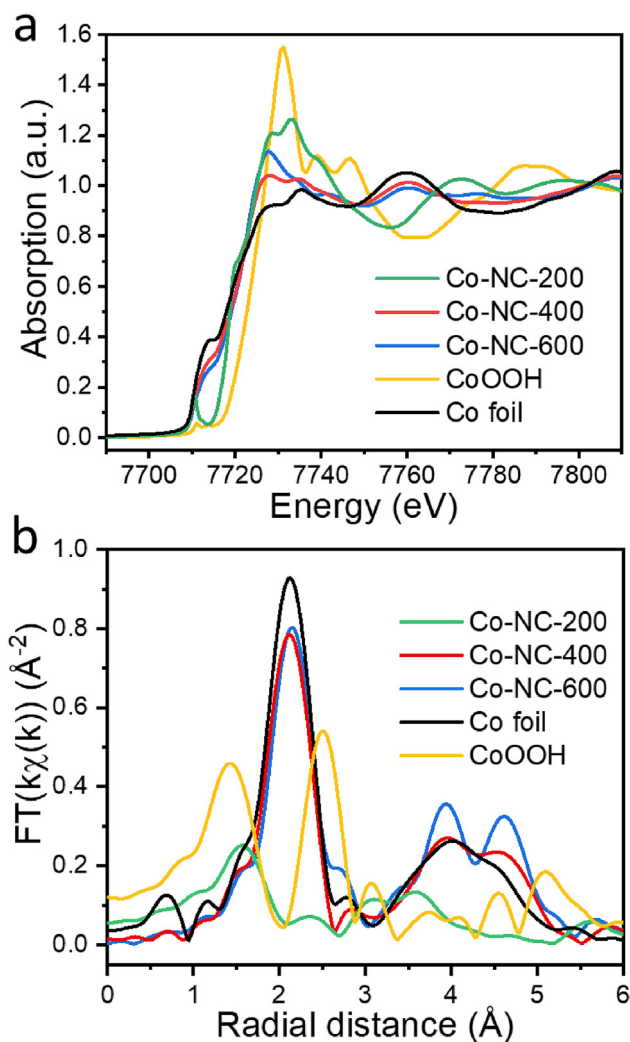
Fig. 4. Co K-edge (a) XANES and (b) the corresponding EXAFS of Co-NC-200, Co-NC-400, and Co-NC-600.

shoulder in both Co-NC-400 and Co-NC-600, which actually featured an intense peak at 2.10 Å, due to the Co–Co bonds of metallic Co, and two minor ones at 3.93 and 4.60 Å, all consistent with those of Co foil [55]. From the fitting results (Figs. S7-S11, Tables S6-S10), it can be seen that Co-NC-400 and Co-NC-600 exhibited a Co–Co bond length of 2.49 Å and a close coordination number (CN) of 7.81 and 8.07, respectively. These CN values are smaller than that of Co foil (12), possibly due to the much smaller sizes of the nanoparticles (Fig. 2). Meanwhile the CN of Co–N/O was ca. 5.24 for Co-NC-200, slightly larger than the theoretical value (4) of the Co–N bonds in ZIF-67, likely due to the partial oxidation/decomposition of the precursor. Taken together, these results are consistent with those from the above TEM and XPS measurements.

3.2. Electrocatalytic activity

Electrochemical measurements were then carried out to evaluate and compare the electrocatalytic activity. Fig. S12 shows the cyclic voltammograms (CVs) of the sample series within the non-Faradaic potential range of -0.1 to $+1.1$ V. It can be seen that the double-layer charging currents were significantly lower for Co-NC-200 and Co-NC-300 than for Co-NC-400, Co-NC-500, and Co-NC-600 (Co-NC-600 also shows a small anodic peak at $+0.4$ V due to the oxidation of surface metallic cobalt [56]). In fact, the electrode double-layer capacitances (C_{dl}) can be estimated to be 3.34 mF cm^{-2} for Co-NC-200 and 2.51 mF cm^{-2} for

Co-NC-300, reached the highest at 86.19 mF cm^{-2} for Co-NC-400, and then decreased slightly to 79.92 mF cm^{-2} for Co-NC-500 and 77.25 mF cm^{-2} for Co-NC-600 (Fig. S13). This suggests that Co-NC-400 possessed the highest electrochemical surface area (ECSA), a unique feature conducive to the accessibility of the catalytic active sites and the eventual electrocatalytic activity.

The OER polarization curves in 1 M KOH are depicted in Fig. 5a. One can see that similar to commercial RuO$_2$, all Co-NC nanocomposites exhibited a sharp increase of the voltammetric current with a positive sweep of the electrode potential beyond $+1.4$ V, suggesting apparent OER activity. Yet, the OER activity varies among the samples. In fact, Co-NC-400 can be seen to stand out as the best OER catalyst amongst the series, with an η_{10} of $+308$ mV and η_{200} of $+410$ mV. The overpotentials are much higher for Co-NC-200 ($+364$ mV and over $+600$ mV), Co-NC-300 ($+340$ mV and $+500$ mV), Co-NC-500 ($+330$ mV and $+530$ mV) and Co-NC-600 ($+347$ mV and over $+600$ mV), whereas for commercial RuO$_2$, $+230$ mV and $+450$ mV (Fig. S14). That is, 400 A turned out to be the optimal heating current for the ultrafast treatment of ZIF-67, and Co-NC-400 even outperformed RuO$_2$ at high current densities (e.g., over 150 mA cm^{-2}) as well as relevant Co-based nanocomposites reported recently in the literature (Table S11).

The Tafel plots are shown in Fig. 5b. One can see that Co-NC-400 featured a Tafel slope of 99.6 mV dec^{-1}, Co-NC-200 displayed a similar one at 98.2 mV dec^{-1}, whereas for Co-NC-300, Co-NC-500, and Co-NC-600, their Tafel slopes are markedly higher at 115.9 mV dec^{-1}, 135.4 mV dec^{-1}, 133.7 mV dec^{-1}, respectively (Fig. 5b). This suggests that the Co-NC-400 sample possessed the most facile electron-transfer kinetics in OER as compared to other samples in the series. In addition, RuO$_2$ can be seen to display a low Tafel slope (47.5 mV dec^{-1}) in the low overpotential region ($+1.40$ to $+1.50$ V vs. RHE), but a markedly higher one at 174.9 mV dec^{-1} at high overpotentials, suggesting sluggish kinetics in producing high OER currents [57]. Consistent results were obtained from electrochemical impedance spectroscopy (EIS) measurements. From the Nyquist plots acquired at the overpotential of $+300$ mV (Fig. 5c), one can see that Co-NC-400 exhibited the lowest charge transfer resistance ($R_{ct} = 15.33$ Ω), as compared to 25.67 Ω for Co-NC-600, and 42.62 Ω for CO-NC-200.

The nanocomposites also manifested excellent stability towards OER. One can see from Fig. 5d that at the overpotential of η_{20}, Co-NC-400 retained its initial current density for 20 h without an apparent decay (the slight fluctuation was due to the accumulation of oxygen bubbles on the electrode surface, and the currents were recovered once the bubbles were shaken off); and the corresponding polarization curves showed a negligible shift over time (Fig. 5e). In contrast, Co-NC-200 actually exhibited an increase of the current density in the first 2 h and then maintained it for the next 18 h. The polarization curve also showed a negative shift in the first 5 h and a slightly positive shift after 20 h, implying electrochemical activation likely due to a significant structural rearrangement (recall that the sample involved only incomplete decomposition of ZIF-67). Co-NC-600 also possessed a rather stable i-t profile for 20 h; and the polarization curve remained virtually unchanged in the first 5 h, but showed a significant negative shift after 10 h, denoting drastic structural dynamics. As for commercial RuO$_2$, both the i-t profile (Fig. 5d) and polarization curves (Fig. 5e) exhibit a substantial decay (ca. 34% of the initial current was lost at 20 h), signifying structural instability during prolonged operation. These results indicate that the Co-NC samples possessed markedly enhanced stability toward OER, as compared to commercial RuO$_2$.

Notably, when Co-NC-400 was subject to acid leaching in 0.5 M H$_2$SO$_4$ at 80 °C for 8 h, the OER activity diminished significantly (Fig. S15), with η_{10} increased to $+440$ mV and η_{200} to ca. $+600$ mV. TEM measurements showed that almost all nanoparticles vanished after the acid treatment (Fig. S16). Concurrently, the peaks of metallic Co and metal-O disappeared from the Co 2p and O 1s XPS spectra, whereas Co^{2+} and N remained detectable, suggesting retention of the CoN$_x$ moieties in the carbon matrix (Fig. S17). This implies that the OER activity was
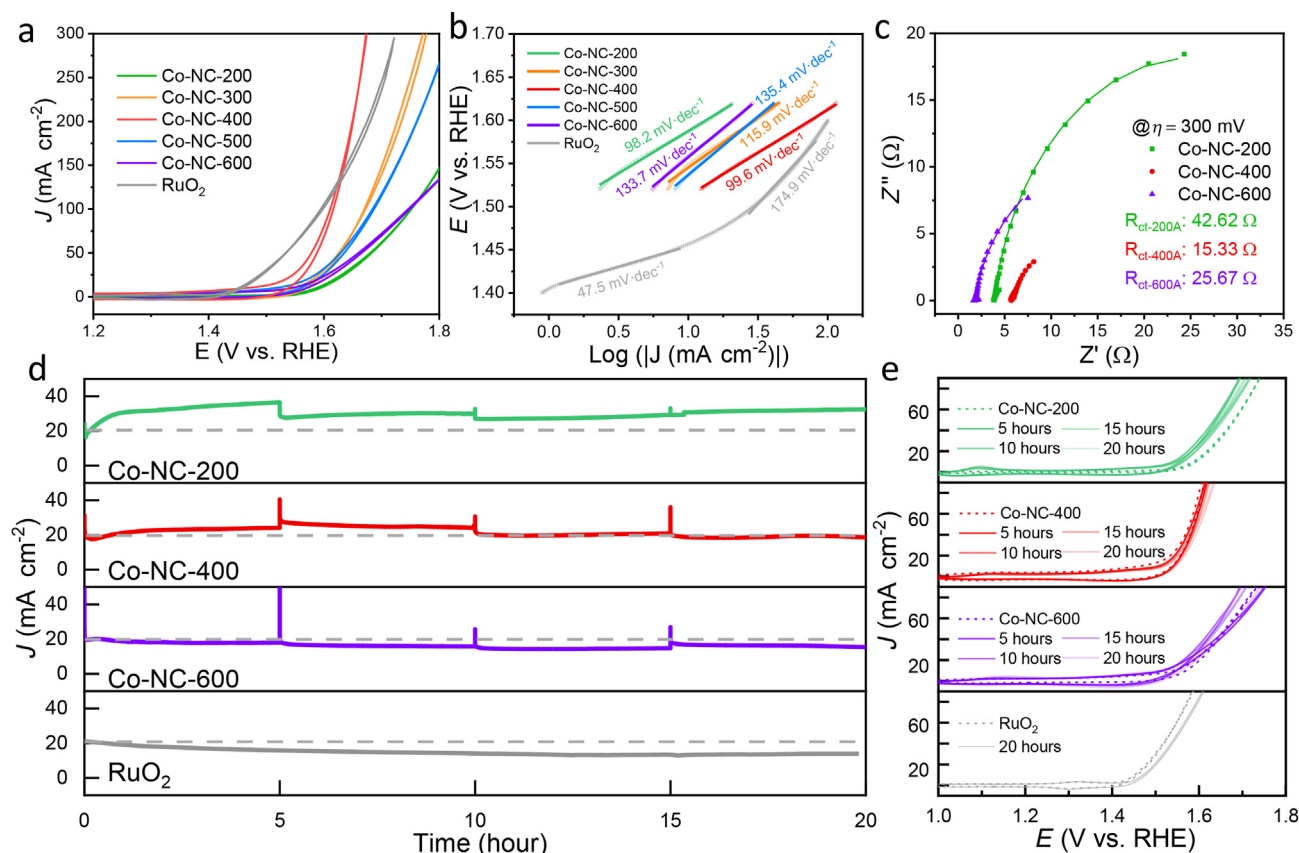
Fig. 5. (a) OER Polarization curves of the sample series and commercial RuO$_2$ in 1 M KOH with a scan rate of 10 mV s^{-1}. (b) Tafel plots of the Co-NC samples and RuO$_2$. (c) Nyquist plots of Co-NC-200, Co-NC-400, and Co-NC-600 at the overpotential of +300 mV. (d) Stability tests by i-t measurements of Co-NC-200, Co-NC-400, Co-NC-600, and RuO$_2$ at their respective η_{20} for 20 h. Note that bubbles were removed from the sample surface every 5 h (e) OER polarization curves of Co-NC-200, Co-NC-400, Co-NC-600, and RuO$_2$ acquired at different time points during the stability tests.

primarily due to the Co/CoO nanoparticles, with only a minimal contribution from the CoN$_x$ moieties.

3.3. Mechanistic study

To further unravel the mechanistic origin of the OER activity, XPS measurements were carried out with three select Co-NC samples (Co-NC-200, Co-NC-400 and Co-NC-600) after 10 scans of the OER polarization curves. From the Co 2p spectra in Fig. S18, all three samples can be seen to exhibit a primary peak at ca. 779 eV, suggesting the formation of Co^{3+} species, most likely due to the oxidation of Co at high electrochemical potentials, and concurrently the disappearance of the 777.8 eV peak indicates the total absence of metallic Co^0 on the sample surface. In addition, the binding energy of the Co^{2+} 2p electrons remained lower in Co-NC-400 and Co-NC-600 than in Co-NC-200. Note that such electron-enriched sites are preferred for OER. This is because in an electron-rich state, the d electrons of Co may extend across the Fermi level, creating half-occupancy e$_g$ orbitals for the Co atoms, which facilitates the coupling of the *OH groups, promotes proton-coupled electron transfer, and enhances the chemisorption of *OOH intermediates and hence O$_2$ production [46,58]. From the O 1s spectra (Fig. S19), a new peak can be seen to emerge at ca. 528.8 eV for all three samples, which can be ascribed to the O atoms in oxyhydroxides (OOH) [43], suggesting the formation of CoOOH species on the catalyst surface. Notably, the total content of the Co species was similar at ca. 10 at% for Co-NC-200 and Co-NC-400, but drastically lower at 7.4 at% for Co-NC-600 (Fig. S20), which were all much higher than those of their as-produced counterparts (Tables S1, S3 and S5). This surface enrichment of the Co species suggests that a dissolution-redeposition process likely occurred during OER

operation [59]. Furthermore, from the N 1s spectra (Fig. S21), one can see that the contents of the N species diminished significantly after OER electrochemistry, from 18.16 to 5.43 at% for Co-NC-200, 7.96 to 1.48 at % for Co-NC-400, and 4.73 to 1.51 at% for Co-NC-600. This implies that the N species (i.e., CoN$_x$ moieties) were unlikely the major contributors to the high and stable OER performance, in accord with results from the acid-etching experiment (Figure S15).

Consistent results were acquired in TEM measurements. As shown in Fig. S22, Co-NC-200 completely collapsed into flaky-like structures after the OER tests, exhibiting clear lattice fringes with a d spacing of 0.198 nm that is consistent with the (104) facets of CoOOH [60]. By contrast, the carbon scaffold of Co-NC-400 retained the original structure and facilitated the formation of abundant CoOOH species on the sample surface (Fig. S23). Co-NC-600 exhibited a similar phenomenon with the formation of CoOOH (Fig. S24). Nevertheless, the amount of CoOOH species was apparently lower than that in Co-NC-400, likely because the high degree of graphitization limited the access of the encapsulated Co/CoO nanoparticles to electrolyte solutions and hence the oxidation into CoOOH. This is indeed confirmed in operando XAS measurements (Figure S25), as detailed below.

Fig. 6a shows the Co K-edge XANES profiles of Co-NC-400 acquired with the electrode potentials varied from open circuit potential (OCP) to +1.6 V. One can see from the figure inset that the absorption edge shifted slightly to a higher energy upon the application of a higher electrode potential, suggesting an increase of the Co valence state. In the corresponding EXAFS profiles in Fig. 6b, the peak of the metallic Co–Co bonds (2.1 Å) can be seen to diminish in intensity, and concurrently, that of the Co–O bonds (at ca. 1.4 Å) became intensified, with increasingly positive electrode potentials, suggesting that metallic co-
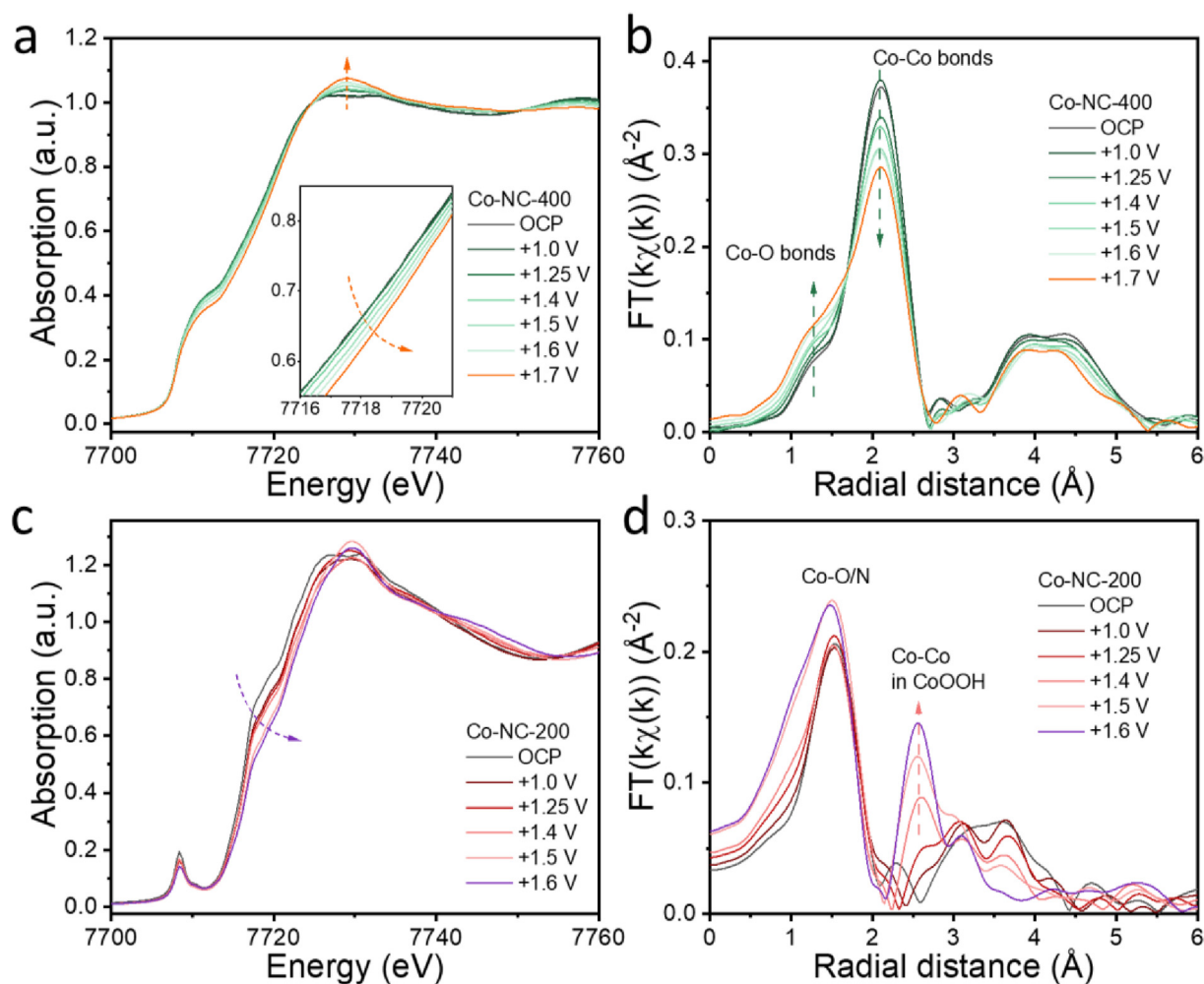
Fig. 6. Operando XAS measurements of Co-NC-400 and Co-NC-200. (a) XANES of Co-NC-400 at different electrochemical potentials and (b) their corresponding EXAFS curves. (c) XANES of Co-NC-200 at different electrochemical potentials and (d) their corresponding EXAFS curves.

balt was slowly converted into CoOOH species, consistent with results from ex situ XPS and TEM measurements (Figures S18, S19 and S23). The fitting results are shown in Fig. S26-S27 and Table S12, where the CN of Co–Co can be seen to decrease from 6.13 to 4.01 while that of Co–O increased from 2.25 to 4.88, consistent with the oxidation of metallic Co into Co–O species under high electrode potentials. As for Co-NC-200 (Fig. 6c), one can see the absorption edge shifted to a significantly higher energy upon the application of a more positive electrode potential, indicating that Co-NC-200 was more susceptible to electrochemical oxidation, most likely due to a low degree of carbonization, as compared to Co-NC-400 and Co-NC-600. Fig. 6d shows the corresponding EXAFS curves, which can be seen to evolve into a profile resembling that of CoOOH (Fig. 4b) with the application of increasingly positive potentials, indeed confirming a ready transformation into CoOOH by electrochemical oxidation. In fact, one can see that a new peak appeared at 2.55 Å at +1.25 V and migrated to 2.71 Å at +1.6 V, which can be assigned to the Co–Co path in CoOOH, and the peak became intensified at higher potentials, due to the formation of a larger amount of CoOOH, as observed in TEM measurements (Fig. S22). Fittings of the EXAFS data (Figs. S28, S29, and Table S13) showed that the CN of Co–O/N increased from 4.08 to 6.03, signifying the conversion of the Co–N_4 moieties into the Co–O_6 units in CoOOH.

Note that each scan in operando XAS measurements took ca. 20 min, which might be insufficient for the materials to undergo a thorough phase transformation. To further probe the valency and structural changes that occurred at high potentials, ex situ XAS measurements were conducted

with Co-NC-200, Co-NC-400, and Co-NC-600 after continuous OER operation for 20 h. As shown in Fig. S30, Co-NC-200 can be seen to exhibit an absorption edge similar to that of CoOOH, and Co-NC-400 and Co-NC-600 showed a marked increase of the absorption edge energy towards that of CoOOH, as compared to their as-prepared ones, consistent with the positive shift of the Co 2p binding energy as observed in XPS measurements (Fig. S18). Analysis of the EXAFS profiles (Fig. S31) and the corresponding fitting results (Fig. S32-S34, Table S14-S16) further elucidated that Co-NC-200 was transformed into CoOOH. Interestingly, Co-NC-400 and Co-NC-600 completely lost their metallic features, with no more Co–Co peaks at around 2.10 Å. This suggests that metallic Co is unlikely to contribute to the OER activity. Meanwhile, both samples exhibited a peak at 2.91 Å, due to the Co at the octahedral site of Co^{III}–O_6 and Co at the tetrahedral site of Co^{II}–O_4, which was not found in Co-NC-200. In fact, such a feature normally exists in Co_3O_4 spinels [54,61]. This suggests that the metallic Co was electrochemically transformed into Co^{II}–O_4 during the prolonged operation, and the produced CoOOH species was responsible for the observed OER activity by facilitating the adsorption of oxygen intermediates [62]. This was most likely aided by the defective carbon shells that encapsulated the Co/CoO nanoparticles such that accessibility by electrolyte species was not completely impeded.

4. Conclusions

In summary, MIH was successfully exploited for the ultrafast preparation of Co-NC nanocomposites from ZIF-67 where Co/CoO

nanoparticles were encapsulated with defective N-doped carbon layers. The sample prepared at 400 A for 10 s, Co-NC-400, was found to exhibit the best performance towards OER in alkaline media, with a low η_{10} of +308 mV and η_{200} of +410 mV, and even outperformed commercial RuO_2 at high overpotentials and relevant Co-based nanocomposites reported recently in the literature. The combined results from ex situ and operando microscopic and spectroscopic measurements showed that metallic Co species were electrochemically transformed into CoOOH, which acted as the catalytic active sites, and the activity was likely enhanced by charge transfer from the graphitized carbon shells that was also responsible for the excellent stability of the nanocomposite catalysts. Results from this study underline the unique significance of MIH in the design and engineering of high-performance electrocatalysts from low-cost precursors (Fig. S35).

Declaration of competing interest

The authors declare that they have no known competing financial interests or personal relationships that could have appeared to influence the work reported in this paper.

Acknowledgement

Appendix A. Supplementary data

Supplementary data to this article can be found online at https://doi.org/10.1016/j.asems.2023.100046.

References

[1] A. Haryanto, S. Fernando, N. Murali, S. Adhikari, Current status of hydrogen production techniques by steam reforming of ethanol: a review, Energy Fuel. 19 (2005) 2098–2106.

[2] J.A. Turner, Sustainable hydrogen production, Science 305 (2004) 972–974.

[3] Z.W. Seh, J. Kibsgaard, C.F. Dickens, I.B. Chorkendorff, J.K. Norskov, T.F. Jaramillo, Combining theory and experiment in electrocatalysis: insights into materials design, Science 355 (2017), eaad4998.

[4] P.Z. Chen, X.L. Hu, High-efficiency anion exchange membrane water electrolysis employing non-noble metal catalysts, Adv. Energy Mater. 10 (2020), 2002285.

[5] T. Reier, M. Oezaslan, P. Strasser, Electrocatalytic oxygen evolution reaction (OER) on Ru, Ir, and Pt catalysts: a comparative study of nanoparticles and bulk materials, ACS Catal. 2 (2012) 1765–1772.

[6] Y. Peng, Q.M. Liu, B.Z. Lu, T. He, F. Nichols, X. Hu, T. Huang, G. Huang, L. Guzman, Y. Ping, S.W. Chen, Organically capped iridium nanoparticles as high-performance bifunctional electrocatalysts for full water splitting in both acidic and alkaline media: impacts of metal-ligand interfacial interactions, ACS Catal. 11 (2021) 1179–1188.

[7] K. Sheng, Q.F. Yi, A.L. Chen, Y.B. Wang, Y.H. Yan, H.D. Nie, X.L. Zhou, CoNi nanoparticles supported on N-doped bifunctional hollow carbon composites as high-performance ORR/OER catalysts for rechargeable Zn-air batteries, ACS Appl. Mater. Interfaces 13 (2021) 45394–45405.

[8] H.Y. Guo, Z.W. Fang, H. Li, D. Fernandez, G. Henkelman, S.M. Humphrey, G.H. Yu, Rational design of rhodium-iridium alloy nanoparticles as highly active catalysts for acidic oxygen evolution, ACS Nano 13 (2019) 13225–13234.

[9] C.H. Wang, H.C. Yang, Y.J. Zhang, Q.B. Wang, NiFe alloy nanoparticles with hcp crystal structure stimulate superior oxygen evolution reaction electrocatalytic activity, Angew. Chem., Int. Ed. 58 (2019) 6099–6103.

[10] J.W.D. Ng, M. Garcia-Melchor, M. Bajdich, P. Chakthranont, C. Kirk, A. Vojvodic, T.F. Jaramillo, Gold-supported cerium-doped NiO_x catalysts for water oxidation, Nat. Energy 1 (2016), 16053.

[11] X.T. Yuan, H.X. Ge, X. Wang, C.L. Dong, W.J. Dong, M.S. Riaz, Z.W. Xu, J.X. Zhang, F.Q. Huang, Controlled phase evolution from Co nanochains to CoO nanocubes and their application as OER catalysts, ACS Energy Lett. 2 (2017) 1208–1213.

[12] H.Y. Jin, J. Wang, D.F. Su, Z.Z. Wei, Z.F. Pang, Y. Wang, In situ cobalt-cobalt oxide/N-doped carbon hybrids as superior bifunctional electrocatalysts for hydrogen and oxygen evolution, J. Am. Chem. Soc. 137 (2015) 2688–2694.

[13] N. Wang, S.L. Ning, X.L. Yu, D. Chen, Z.L. Li, J.C. Xu, H. Meng, D.K. Zhao, L.G. Li, Q.M. Liu, B.Z. Lu, S.W. Chen, Graphene composites with Ru-RuO_2 heterostructures: highly efficient Mott-Schottky-type electrocatalysts for pH-universal water splitting and flexible zinc-air batteries, Appl. Catal. B Environ. 302 (2022), 120838.

[14] C.L. Luan, G.L. Liu, Y.J. Liu, L. Yu, Y. Wang, Y. Xiao, H.Y. Qiao, X.P. Dai, X. Zhang, Structure effects of 2D materials on alpha-nickel hydroxide for oxygen evolution reaction, ACS Nano 12 (2018) 3875–3885.

[15] C.G. Kuai, Z.R. Xu, C. Xi, A.Y. Hu, Z.J. Yang, Y. Zhang, C.J. Sun, L.X. Li, D. Sokaras, C.K. Dong, S.Z. Qiao, X.W. Du, F. Lin, Phase segregation reversibility in mixed-metal hydroxide water oxidation catalysts, Nat. Catal. 3 (2020) 743–753.

[16] D. Friebel, M.W. Louie, M. Bajdich, K.E. Sanwald, Y. Cai, A.M. Wise, M.J. Cheng, D. Sokaras, T.C. Weng, R. Alonso-Mori, R.C. Davis, J.R. Bargar, J.K. Norskov, A. Nilsson, A.T. Bell, Identification of highly active Fe sites in (Ni,Fe)OOH for electrocatalytic water splitting, J. Am. Chem. Soc. 137 (2015) 1305–1313.

[17] Y.P. Liu, X. Liang, L. Gu, Y. Zhang, G.D. Li, X.X. Zou, J.S. Chen, Corrosion engineering towards efficient oxygen evolution electrodes with stable catalytic activity for over 6000 hours, Nat. Commun. 9 (2018) 2609.

[18] M.J. Cui, C.P. Yang, B.Y. Li, Q. Dong, M.L. Wu, S. Hwang, H. Xie, X.Z. Wang, G.F. Wang, L.B. Hu, High-entropy metal sulfide nanoparticles promise high-performance oxygen evolution reaction, Adv. Energy Mater. 11 (2021), 2002887.

[19] A. Dutta, N. Pradhan, Developments of metal phosphides as efficient OER precatalysts, J. Phys. Chem. Lett. 8 (2017) 144–152.

[20] Y. Peng, S.W. Chen, Electrocatalysts based on metal@carbon core@shell nanocomposites: an overview, Green Energy Environ. 3 (2018) 335–351.

[21] Y.J. Tang, H. Zheng, Y. Wang, W. Zhang, K. Zhou, Laser-induced annealing of metal-organic frameworks on conductive substrates for electrochemical water splitting, Adv. Funct. Mater. 31 (2021), 2102648.

[22] D.N. Ding, K. Shen, X.D. Chen, H.R. Chen, J.Y. Chen, T. Fan, R.F. Wu, Y.W. Li, Multi-level architecture optimization of MOF-templated Co-based nanoparticles embedded in hollow N-doped carbon polyhedra for efficient OER and ORR, ACS Catal. 8 (2018) 7879–7888.

[23] T. Rodenas, S. Beeg, I. Spanos, S. Neugebauer, F. Girgsdies, G. Algara-Siller, P.P.M. Schleker, P. Jakes, N. Pfander, M. Willinger, M. Greiner, G. Prieto, R. Schlogl, S. Heumann, 2D metal organic framework-graphitic carbon nanocomposites as precursors for high-performance O_2-evolution electrocatalysts, Adv. Energy Mater. 8 (2018), 1802404.

[24] X.J. Cui, P.J. Ren, D.H. Deng, J. Deng, X.H. Bao, Single layer graphene encapsulating non-precious metals as high-performance electrocatalysts for water oxidation, Energy Environ. Sci. 9 (2016) 123–129.

[25] Y. Yang, Z.Y. Lin, S.Q. Gao, J.W. Su, Z.Y. Lun, G.L. Xia, J.T. Chen, R.R. Zhang, Q.W. Chen, Tuning electronic structures of nonprecious ternary alloys encapsulated in graphene layers for optimizing overall water splitting activity, ACS Catal. 7 (2017) 469–479.

[26] C.H. Wang, J. Kim, J. Tang, M. Kim, H. Lim, V. Malgras, J. You, Q. Xu, J.S. Li, Y. Yamauchi, New strategies for novel MOF-derived carbon materials based on nanoarchitectures, Chem 6 (2020) 19–40.

[27] C. Young, J. Wang, J. Kim, Y. Sugahara, J. Henzie, Y. Yamauchi, Controlled chemical vapor deposition for synthesis of nanowire arrays of metal-organic frameworks and their thermal conversion to carbon/metal oxide hybrid materials, Chem. Mater. 30 (2018) 3379–3386.

[28] X. Wang, X.Y. Zhang, G.T. Fu, Y.W. Tang, Recent progress of electrospun porous carbon-based nanofibers for oxygen electrocatalysis, Mater. Today Energy 22 (2021), 100850.

[29] H. Tabassum, A. Mahmood, B.J. Zhu, Z.B. Liang, R.Q. Zhong, S.J. Guo, R.Q. Zou, Recent advances in confining metal-based nanoparticles into carbon nanotubes for electrochemical energy conversion and storage devices, Energy Environ. Sci. 12 (2019) 2924–2956.

[30] Q.M. Liu, Y. Peng, Q.X. Li, T. He, D. Morris, F. Nichols, R. Mercado, P. Zhang, S.W. Chen, Atomic dispersion and surface enrichment of palladium in nitrogen-doped porous carbon cages lead to high-performance electrocatalytic reduction of oxygen, ACS Appl. Mater. Interfaces 12 (2019) 17641–17650.

[31] Q. Hu, G.M. Li, Z. Han, Z.Y. Wang, X.W. Huang, H.P. Yang, Q.L. Zhang, J.H. Liu, C.X. He, Recent progress in the hybrids of transition metals/carbon for electrochemical water splitting, J. Mater. Chem. A 7 (2019) 14380–14390.

[32] J.W. Zhu, S.C. Mu, Defect engineering in the carbon-based electrocatalysts: insight into the intrinsic carbon defects, Adv. Funct. Mater. 30 (2020), 2001097.

[33] S.H. Lee, J. Kim, D.Y. Chung, J.M. Yoo, H.S. Lee, M.J. Kim, B.S. Mun, S.G. Kwon, Y.E. Sung, T. Hyeon, Design principle of Fe-N-C electrocatalysts: how to optimize multimodal porous structures? J. Am. Chem. Soc. 141 (2019) 2035–2045.

[34] Q.M. Liu, S.W. Chen, Ultrafast synthesis of electrocatalysts, Trends Chem. 4 (2022) 918–934.

[35] Q.M. Liu, B.Z. Lu, F. Nichols, J. Ko, R. Mercado, F. Bridges, S.W. Chen, Rapid preparation of carbon-supported ruthenium nanoparticles by magnetic induction

heating for efficient hydrogen evolution reaction in both acidic and alkaline media, SusMat 2 (2022) 335–346.

[36] B.Z. Lu, Q.M. Liu, C. Wang, Z. Masood, D.J. Morris, F. Nichols, R. Mercado, P. Zhang, Q.F. Ge, H.L. Xin, S.W. Chen, Ultrafast preparation of nonequilibrium FeNi spinels by magnetic induction heating for unprecedented oxygen evolution electrocatalysis, Research 2022 (2022), 9756983.

[37] Y.G. Yao, Z.N. Huang, P.F. Xie, S.D. Lacey, R.J. Jacob, H. Xie, F.J. Chen, A.M. Nie, T.C. Pu, M. Rehwoldt, D.W. Yu, M.R. Zachariah, C. Wang, R. Shahbazian-Yassar, J. Li, L.B. Hu, Carbothermal shock synthesis of high-entropy-alloy nanoparticles, Science 359 (2018) 1489–1494.

[38] D.X. Luong, K.V. Bets, W.A. Algozeeb, M.G. Stanford, C. Kittrell, W. Chen, R.V. Salvatierra, M.Q. Ren, E.A. McHugh, P.A. Advincula, Z. Wang, M. Bhatt, H. Guo, V. Mancevski, R. Shahsavari, B.I. Yakobson, J.M. Tour, Gram-scale bottom-up flash graphene synthesis, Nature 577 (2020) 647–651.

[39] C. Meng, M.C. Lin, X.C. Sun, X.D. Chen, X.M. Chen, X.W. Du, Y. Zhou, Laser synthesis of oxygen vacancy-modified CoOOH for highly efficient oxygen evolution, Chem. Commun. 55 (2019) 2904–2907.

[40] R. Jiang, Y.M. Da, X.P. Han, Y.A. Chen, Y.D. Deng, W.B. Hu, Ultrafast synthesis for functional nanomaterials, Cell Rep. Phys. Sci. 2 (2021), 100302.

[41] J.F. Yao, M. He, K. Wang, R.Z. Chen, Z.X. Zhong, H.T. Wang, High-yield synthesis of zeolitic imidazolate frameworks from stoichiometric metal and ligand precursor aqueous solutions at room temperature, CrystEngComm 15 (2013) 3601–3606.

[42] X. Miao, D. Qu, D.X. Yang, B. Nie, Y.K. Zhao, H.Y. Fan, Z.C. Sun, Synthesis of carbon dots with multiple color emission by controlled graphitization and surface functionalization, Adv. Mater. 30 (2018), 1704740.

[43] W.R. Zheng, M.J. Liu, L.Y.S. Lee, Electrochemical instability of metal-organic frameworks: in situ spectroelectrochemical investigation of the real active sites, ACS Catal. 10 (2020) 81–92.

[44] W.H. He, R. Ifraemov, A. Raslin, I. Hod, Room-temperature electrochemical conversion of metal-organic frameworks into porous amorphous metal sulfides with tailored composition and hydrogen evolution activity, Adv. Funct. Mater. 28 (2018), 1707244.

[45] Y. Jia, L.Z. Zhang, A.J. Du, G.P. Gao, J. Chen, X.C. Yan, C.L. Brown, X.D. Yao, Defect graphene as a trifunctional catalyst for electrochemical reactions, Adv. Mater. 28 (2016) 9532–9538.

[46] F.M. Tang, W.R. Cheng, Y.Y. Huang, H. Su, T. Yao, Q.H. Liu, J.K. Liu, F.C. Hu, Y. Jiang, Z.H. Sun, S.Q. Wei, Strong surface hydrophilicity in Co-based electrocatalysts for water oxidation, ACS Appl. Mater. Interfaces 9 (2017) 26867–26873.

[47] T. Sharifi, G. Hu, X.E. Jia, T. Wagberg, formation of active sites for oxygen reduction reactions by transformation of nitrogen functionalities in nitrogen-doped carbon nanotubes, ACS Nano 6 (2012) 8904–8912.

[48] Y.Y. Song, T. He, Y.L. Zhang, C.Y. Yin, Y. Chen, Q.M. Liu, Y. Zhang, S.W. Chen, Cobalt single atom sites in carbon aerogels for ultrasensitive enzyme-free electrochemical detection of glucose, J. Electroanal. Chem. 906 (2022), 116024.

[49] T. He, Y. Peng, Q.X. Jia, J.E. Lu, Q.M. Liu, R. Mercado, Y. Chen, F. Nichols, Y. Zhang, S.W. Chen, Nanocomposites based on ruthenium nanoparticles supported on cobalt and nitrogen-codoped graphene nanosheets as bifunctional catalysts for electrochemical water splitting, ACS Appl. Mater. Interfaces 11 (2019) 46912–46919.

[50] B.Z. Lu, Q.M. Liu, F. Nichols, R. Mercado, D. Morris, N. Li, P. Zhang, P. Gao, Y. Ping, S.W. Chen, Oxygen reduction reaction catalyzed by carbon-supported platinum few-atom clusters: significant enhancement by doping of atomic cobalt, Research 2020 (2020), 9167829.

[51] X.L. Huang, R.Z. Wang, D. Xu, Z.L. Wang, H.G. Wang, J.J. Xu, Z. Wu, Q.C. Liu, Y. Zhang, X.B. Zhang, Homogeneous CoO on graphene for binder-free and ultralong-life lithium ion batteries, Adv. Funct. Mater. 23 (2013) 4345–4353.

[52] S.K. Pandey, A. Kumar, S. Khalid, A.V. Pimpale, Electronic states of LaCoO₃: Co K-edge and La L-edge x-ray absorption studies, J. Phys. Condens. Matter 18 (2006) 7103.

[53] D.J. SantaLucia, W.H. Hu, D.N. Wang, J. Huang, J.F. Berry, Postsynthetic treatment of ZIF-67 with 5-methyltetrazole: evolution from pseudo-T_d to pseudo-O_h symmetry and collapse of magnetic ordering, Inorg. Chem. 61 (2022) 6056–6062.

[54] B. Seo, Y.J. Sa, J. Woo, K. Kwon, J. Park, T.J. Shin, H.Y. Jeong, S.H. Joo, Size-dependent activity trends combined with in situ X-ray absorption spectroscopy reveal insights into cobalt oxide/carbon nanotube-catalyzed bifunctional oxygen electrocatalysis, ACS Catal. 6 (2016) 4347–4355.

[55] I. Arcon, A. Tuel, A. Kodre, G. Martin, A. Barbier, EXAFS determination of the size of Co clusters on silica, J. Synchrotron Radiat. 8 (2001) 575–577.

[56] A. Holewinski, J.C. Idrobo, S. Linic, High-performance Ag-Co alloy catalysts for electrochemical oxygen reduction, Nat. Chem. 6 (2014) 828–834.

[57] K.A. Stoerzinger, L. Qiao, M.D. Biegalski, Y. Shao-Horn, Orientation-dependent oxygen evolution activities of rutile IrO₂ and RuO₂, J. Phys. Chem. Lett. 5 (2014) 1636–1641.

[58] Z.Y. Lu, H.T. Wang, D.S. Kong, K. Yan, P.C. Hsu, G.Y. Zheng, H.B. Yao, Z. Liang, X.M. Sun, Y. Cui, Electrochemical tuning of layered lithium transition metal oxides for improvement of oxygen evolution reaction, Nat. Commun. 5 (2014) 4345.

[59] C. Stumm, M. Bertram, M. Kastenmeier, F.D. Speck, Z.Z. Sun, J. Rodriguez-Fernandez, J.V. Lauritsen, K.J.J. Mayrhofer, S. Cherevko, O. Brummel, J. Libuda, Structural dynamics of ultrathin cobalt oxide nanoislands under potential control, Adv. Funct. Mater. 31 (2021), 2009923.

[60] B. Zhang, J.W. Shan, W.L. Wang, P. Tsiakaras, Y.Y. Li, Oxygen vacancy and core-shell heterojunction engineering of anemone-like CoP@CoOOH bifunctional electrocatalyst for efficient overall water splitting, Small 18 (2022), 2106012.

[61] F. Reikowski, F. Maroun, I. Pacheco, T. Wiegmann, P. Allongue, J. Stettner, O.M. Magnussen, Operando surface X-ray diffraction studies of structurally defined Co₃O₄ and CoOOH thin films during oxygen evolution, ACS Catal. 9 (2019) 3811–3821.

[62] H.Y. Wang, S.F. Hung, H.Y. Chen, T.S. Chan, H.M. Chen, B. Liu, In operando identification of geometrical-site-dependent water oxidation activity of spinel Co₃O₄, J. Am. Chem. Soc. 138 (2016) 36–39.